32nd Electric Vehicle Symposium (EVS32)
Lyon, France, May 19-22, 2019

Multi-scale modeling of a high performance PEM fuel cell powered highway bus

Marion Georges[1,2], Liangfei Xu[1,**], Bingkun Cai[1], Jiayi Hu[1], Jianqiu Li[1,*], Minggao Ouyang[1]
[1]*State Key Laboratory of Automotive Safety and Energy, Tsinghua University, 100084, Beijing, China*
[2]*Engineering Student at CentraleSuplec, Gif-sur-Yvette 91190, France*
E-mail address: marion.georges@supelec.fr; xuliangfei@tsinghua.edu.cn;
lijianqiu@tsinghua.edu.cn; ouymg@tsinghua.edu.cn;
[*]*Corresponding author: Prof. Jianqiu Li* [**]Co-corresponding author: Dr. Liangfei Xu

Abstract
The next generation of fuel cell buses is being designed as an intercity transportation, increasing lifespan, mileage and hydrogen consumption goals. This Matlab/Simulink modeling work simulates the powertrain of 2022 Beijing Olympic Games prototypes : polymer electrolyte membrane fuel cell powered highway buses.
From vehicle's speed to DC/AC switches state, the modeling includes several sizes and frequencies. Methods employed for the modeling of each components and simple control processes are provided, working points transitions and discretization effects are discussed, and examples of powers, voltages and currents are displayed. Finally an energy flow diagram for the CWTVC driving cycle is given.
Keywords: bus, powertrain, fuel cell, AC motor, DC-DC

1 Introduction

Polymer electrolyte membrane (PEM) fuel cells have advantages of high efficiency, low noise and zero emission, and are considered a major player of power sources in the future electrification of transportation [1, 2, 3, 4]. China has been developing its fuel cell city buses since 2001. The next generation of fuel cell buses is being designed as an intercity transportation. This research work is carried out within the framework of a National Key R&D Program of China. Several prototype high performance PEM fuel cell powered highway buses will be manufactured and launched for the 2022 Beijing Olympic Games, connecting Beijing and Zhangjiakou (200 km). Using the software Matlab/Simulink [5], this research work focuses on the multi-scale modeling of such electric hybrid powertrain.The powertrain has the following architecture (see Fig.1): a fuel cell system, a DC/DC converter, an alternative path without DC/DC, a battery, a DC/AC converter, a permanent magnet synchronous motor and a transmission.

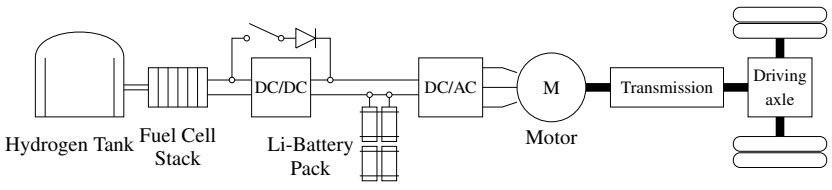

Figure 1: Powertrain structure of the intercity bus

The powertrain modeling will help in the design of oncoming manufactured buses. Requirement specifications for the Powertrain System Research Group's project emphasize a service life of more than 10 000h, with 1000h for the real vehicle test, a 0 to 50km/h acceleration time below 15s, a driving mileage of more than 500km, a 30 minutes maximum speed of 100km/h and an hydrogen consumption of less than 8.0kg per 100km. With a 80kW rated power, the fuel cell engine is expected with a maximum efficiency superior to 55% (including the DC/DC) and also with a low temperature start.
The simulation sample time makes possible an investigation of high frequencies and discretization in the motor drive control, power demand apportionment and battery and fuel cell working points. To this end, characteristic curves for several control steps have to be defined, specific parameters have to be identified

in this process of powertrain design, and effective limitations have to be evaluated.
The modeling deals with different sizes and frequencies (see Fig.2). The bus' speed and the battery state of charge (SOC) are relevant with respect to a half-hour driving cycle while switching of the DC/AC converter gates on a period of 100μs. The simulation higher frequency is a compromise between time computation and model precision. To enhance the fuel cell durability, the fuel cell working point has to be changed smoothly whereas the battery shall meet the needs of power demand, achieving the driver's input. Using averaged currents and voltages for electrical motor drive or reducing the focus on specific powertrain components may dim the link between low frequency factors or components and high frequency ones. This modeling shall determine the relevant driving demands for power, torque, acceleration and braking. At the same time the corresponding specific electrical behavior of powertrain components will be determined. The model will also show where the round up and discretization factors are, what the numerous swift demands for relevant driving are, etc.

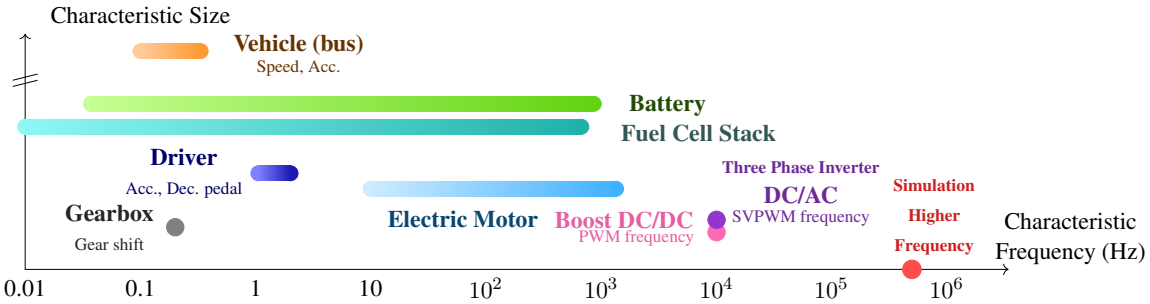

Figure 2: Characteristic sizes and frequencies for the whole powertrain, a multi-scale modeling

At first, details and equations about the modeling of each components are given. This includes the evaluation of the torque at the wheel according to the bus size, a description of the DC side electrical circuit, the characterizations of the fuel cell and battery, the equations of the permanent magnet synchronous motor and an identification of the required motor parameters. Then three control parts are described : (1) the main control loop via the driver pedals travels yielding at the end the target motor torque; (2) the drive motor control including the command of motor currents and DC/AC converter gates switching pattern with space vector pulse width modulation (PWM); (3) the control of the power demand apportionment ensuring the fuel cell slow changes and the command of the DC/DC converter with PWM. Finally three examples of the simulation results are shown and explained. An energy flow diagram of the powertrain is given for a specific high duty vehicles driving cycle.

2 System and Models

2.1 Torque at the wheel

The transmission between the wheel and the motor increases the torque by a coefficient i equal to 34.75 for vehicle speed below 52 km/h and 13.9 above that. The maximum vehicle speed is 130km/h resulting in a maximum rotor speed of 1057rad/s. T_e is the motor torque and α_{gr} the slope of the road.

$$T_{e,wheel} = R_{wheel} * [e\ m_{veh}\ \frac{dv_{veh}}{dt} + m_{veh}\ g\ f_r\ \cos(\alpha_{gr}) + m_{veh}\ g\ \sin(\alpha_{gr}) + c_w\ A_{veh}\ \frac{\rho_L}{2} v_{veh}^2] \quad (1)$$

$$T_{e,wheel} = i\ \eta\ T_e \quad (2) \qquad \omega_{motor} = i\ \omega_{wheel} \quad (3)$$

Table 1: Bus parameters for the road resistance force

Vehicle's mass	m_{veh}	18000 kg	Main profile of the vehicle	A_{veh}	8.16 m^2
Rolling coefficient	f_r	0.012	Inertia coefficient	e	1.05
Drag coefficient	c_w	0.65	Wheel radius	R_{wheel}	0.475 m
Air density	ρ_L	1.2258 kg/m^3	Efficiency of the transmission	η	0.99

2.2 Electrical Circuit

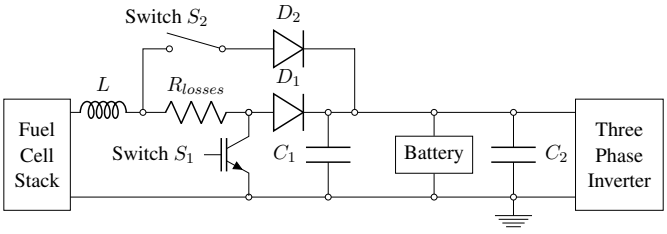

Figure 3: DC side of the electrical circuit in the powertrain

Table 2: Components values

L = 50μH
C1 = 500μF
C2 = 1500μF
R_{losses} = 5mΩ
V_{diode} = 0.8V

The battery directly constrains the voltage of the drive-train. As for the fuel cell, the electrical circuit implements both a load-following mode and a DC/DC mode. The DC/DC is composed of a large capacity,

a diode, an IGBT switch S1, a medium inductance L and a small resistor to model the losses in the converter. The nominal voltages of the fuel cell and the battery are such that the DC/DC voltage gain is quite small (inferior to 1.5). By closing the switch S2, a direct path is made and the voltage of the fuel cell is equal to the battery voltage (minus the diode voltage). The fuel cell and battery power deliveries are then dictated by the motor drive control. Opening the switch S2 and controlling the unidirectional boost DC/DC placed next to the fuel cell transforms the fuel cell voltage into the battery voltage. Higher power, which leads to lower voltage, can then be requested from the fuel cell. Thanks to this configuration, the working point on the fuel cell characteristic curve can be managed; a flat power demand is targeted to enhance the fuel cell life durability. The inductance is placed before the point of bifurcation to smooth the fuel cell current in both cases. Thanks to the diodes D1 and D2, no current is allowed from the battery or from the motor (regenerative braking) in direction of the fuel cell. In theory nothing prevents the motor drive control from inducing current step changes in the DC side. The capacity C2 smooths the demand power for the sources.

2.3 Fuel Cell and Battery

With the help of Matlab/Simulink tools, the previously depicted electrical circuit is easily linked with blocks modeling the fuel cell, battery, three phase inverter and synchronous motor. The characterization of fuel cell and battery is based on the project current selection.
The fuel cell current and voltage are set using a characteristic curve derived from a sample of experimental data. The open circuit voltage is 580V. The voltage curve shows a sharp decrease and then a lower rate decrease as the current increases. i_{fc} and v_{fc} are the quantities which correspond to the fuel cell inputs into the electrical circuit as seen in Fig.3. The fuel cell would deliver a maximum power $i_{fc}v_{fc}$ of 80kW. The Matlab model takes into account the open circuit voltage minus the activation overvoltage and ohmic losses.
The battery is characterized by a nominal voltage at 518V and a rated capacity at 78Ah. The voltage is higher when the battery is charging (i_{bat}<0) than when is discharging (i_{bat}>0). The battery voltage increases with the battery state of charge. The fuel cell and battery working points for the CWTVC driving cycle are shown Fig.4 and Fig.5.

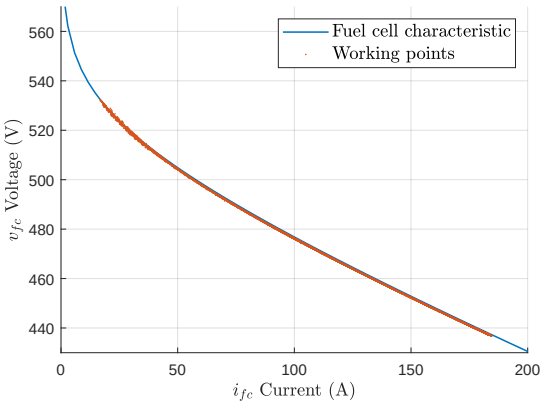

Figure 4: Example of some fuel cell working points

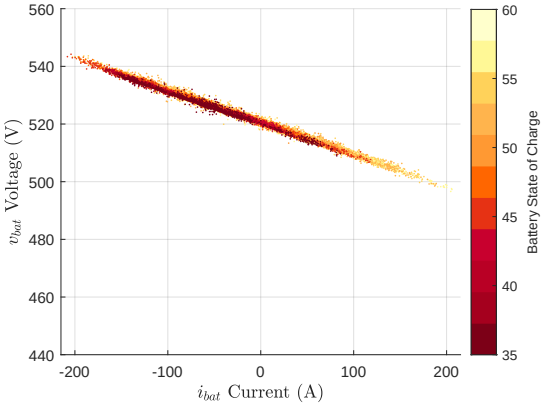

Figure 5: Example of some battery working points

2.4 Interior Permanent Magnet Synchronous Motor

First the motor torque T_e is expressed using d,q quantities. Then the proper working points are expressed to guarantee the current and voltage limits. Afterwards parameters which are needed for the Matlab/Simulink model block are identified. Finally the working points are adapted to keep the motor power below 150kW.

2.4.1 DQ0 Transform

The DQ0 transform is the substitution from the coiling of phases a,b,c whose magnetic axis are idle in regards to the stator, with two imaginary coilings d,q whose magnetic axles are cohesive with the rotor. The three-phase AC quantities v_a,v_b,v_c and i_a,i_b,i_c are turned into two DC quantities v_d,v_q and i_d,i_q. The amplitude invariant DQ0 transformation matrix is given as below :

$$T_{dq0} = \frac{2}{3}\begin{bmatrix} \cos(\theta_{elec}) & \cos(\theta_{elec}-\frac{2\pi}{3}) & \cos(\theta_{elec}-\frac{4\pi}{3}) \\ -\sin(\theta_{elec}) & -\sin(\theta_{elec}-\frac{2\pi}{3}) & -\sin(\theta_{elec}-\frac{4\pi}{3}) \\ \frac{1}{2} & \frac{1}{2} & \frac{1}{2} \end{bmatrix} \quad (4)$$

2.4.2 Electromagnetic torque T_e

The angular rotor speed ω_{motor} of a multipolar triphase synchronous machine is related to the electrical angular speed ω_{elec} by nb_p the pairs of poles, $\omega_{elec} = nb_p\,\omega_{motor}$. The DQ0 transform diagonalizes the inductance matrix and with Φ_f the amplitude of the flux induced by the permanent magnets of the rotor in the stator phases and L_d,L_q the d,q axis inductances, we get :

$$\Phi_d = L_d i_d + \Phi_f \quad (5) \qquad \Phi_q = L_q i_q \quad (6)$$

For an interior permanent magnet synchronous motor (IPMSM), $L_d < L_q$ (7)

With R_s the stator windings resistance :

$$T_e = \frac{3}{2} n b_p [\Phi_f i_q + (L_d - L_q) i_d i_q] \quad (8)$$

$$v_d = L_d \frac{di_d}{dt} - \omega_{elec} L_q i_q + R_s \, i_d \quad (9)$$

$$v_q = L_q \frac{di_q}{dt} + \omega_{elec}(L_d i_d + \Phi_f) + R_s \, i_q \quad (10)$$

2.4.3 Wide Speed Motor Operation

An IPMSM has several operation speed range domains. The working points are adapted to deal with the current limit condition and voltage limit condition :

$$i_{s,max} \geq \sqrt{i_d^2 + i_q^2} \quad (11) \qquad v_{s,max} \geq \sqrt{v_d^2 + v_q^2} \quad (12)$$

From (9) and (10), in steady state and with the resistance R_s neglected, the voltage limit condition is:

$$\omega_{elec} \leq \frac{v_{s,max}}{\sqrt{(L_d i_d + \Phi_f)^2 + (L_q i_q)^2}} \quad (13)$$

In the plane (i_d,i_q), the voltage limit condition is an ellipse of center ($\frac{-\Phi_f}{L_d}$, 0) whose area decreases as the speed increases (see Fig.6). Ideally the working points (i_d,i_q) are chosen with the smallest stator current i_s (equal to $\sqrt{i_d^2 + i_q^2}$). For low speed, getting the smallest stator current defines a characteristic called the Maximum Torque per Ampere (MTPA) [6]. In the plane (i_d,i_q), let us call point A ($i_{d,A}$,$i_{q,A}$) the intersection point between the MTPA curve, the current limit condition ($i_{s,max}$ radius circle) and the voltage limit condition (ellipse). $\omega_{elec,A}$ is the maximum angular electrical speed of the constant torque region. Below $\omega_{elec,A}$, the working point (i_d,i_q) evolves along the MTPA curve, expressed by :

$$i_d = \frac{\Phi_f}{2(L_q - L_d)} - \sqrt{\frac{\Phi_f^2}{4(L_q - L_d)^2} + i_q^2} \quad (14)$$

Above $\omega_{elec,A}$, the flux weakening strategy is used. The effective stator flux linkage Φ_d, expressed by (5), is reduced with negative d-axis stator current i_d.

With the assumption the working points are chosen at the border of each voltage limit ellipses to obtain the smallest stator current, with (8) and (13), constant P_m power curves could be expressed by:

$$i_d = \Phi_f \frac{\left[(\frac{3}{2}\frac{v_{s,max}}{P_m} i_q)^2 (L_q - L_d) + L_d\right] - L_q \sqrt{(\frac{3}{2}\frac{v_{s,max}}{P_m} i_q)^2 (1 + (\frac{(L_d - L_q) i_q}{\Phi_f})^2) - (\frac{L_d i_q}{\Phi_f})^2}}{\left[(\frac{3}{2}\frac{v_{s,max}}{P_m} i_q)^2 (L_d - L_q)^2 - L_d^2\right]} \quad (15)$$

The form of the constant power curves changes in function of Φ_f, L_d and $i_{s,max}$ [6]. The following equality is chosen :

$$\Phi_f = L_d i_{s,max} \quad (16)$$

Moving along the current limit curve ($i_{s,max}$ radius circle) and only decreasing the torque to match the voltage limit condition gives the maximum reachable torques at high speed, that is to say the maximum reachable powers P_m. The current limit curve is expressed by :

$$i_d = \frac{L_d \Phi_f - \sqrt{L_d^2 \Phi_f^2 + (L_q^2 - L_d^2)(L_q^2 i_{s,max}^2 + \Phi_f^2 - (\frac{v_{s,max}}{\omega_{elec}})^2)}}{(L_q^2 - L_d^2)} \quad (17)$$

2.4.4 Motor Parameters Identification

Table 3: Project specifications for the motor

Interior Permanent Magnet Synchronous Motor (IPMSM)	Maximum Power $P_{m,max}$	150 kW (designed for 180 kW)
	Maximum Torque $T_{e,max}$	1500 Nm
	Pairs of poles nb_p	8
	Base angular rotor speed $\omega_{motor,A} = P_{m,max}/T_{e,max}$	100 rad/s (designed for 120 rad/s)
	Base angular electrical speed $\omega_{elec,A} = nb_p \, \omega_{motor,A}$	800 rad/s (designed for 960 rad/s)

Starting from Table 3 and the previous equations, it is possible to solve for lacking parameters. In anticipation, a cross-reference has been conducted with pre-simulations - to know more about $i_{s,max}$ and $v_{s,max}$ dependent of the powertrain's electrical circuit - and with earlier experimentation data on similar IPMSMs - to get R_s and to know more about the ranges of L_d, L_q and Φ_f. By expressing ($i_{d,A}$,$i_{q,A}$) in (8), (11), (12) and (14), adding some limitation on the parameters range and respecting (7) and (16), we get all the motor parameters.

Table 4: Identified Parameters

Φ_f = 0.18 Wb	R_s = 0.035 Ω	L_d = 0.335 mH	L_q = 0.665 mH
$i_{d,A}$ = -270 A	$i_{q,A}$ = 464.5 A	$i_{s,max}$ = 535 A	$v_{s,max}$ = 306 V

2.4.5 Voltage limit ellipses, constant torque curves and constant power curves

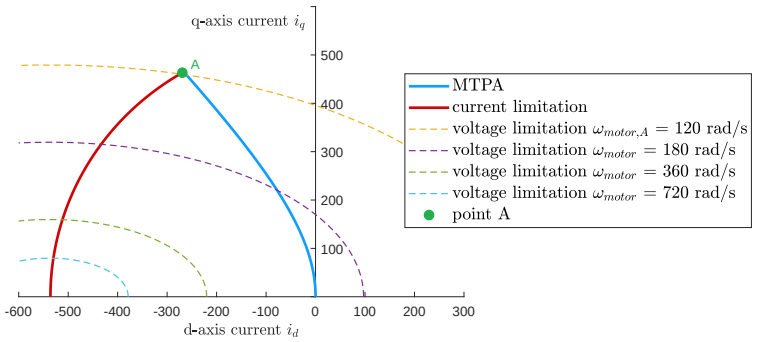

Figure 6: MTPA curve, current limitation and voltage limitation in function of ω_{motor} in the plane (i_d,i_q)

The specific application we have for this motor is $T_e\omega_{motor} \leq P_{m,max}$ with $P_{m,max} = T_{e,A}\omega_{motor,A}$. With the knowledge of the actual motor speed, for example equal to 180rad/s (see Fig.7), the voltage limitation ellipse is known. Taking the maximum achievable torque with the working point at the current limit curve gives the power equal to 220kW, superior to $P_{m,max}$. The torque which corresponds to the $P_{m,max}$ constant power curve is 1000Nm. In practice, in the plane (i_d,i_q), all the motor working points would belong in the area defined between the MTPA curve and the $P_{m,max}$ constant power curve.

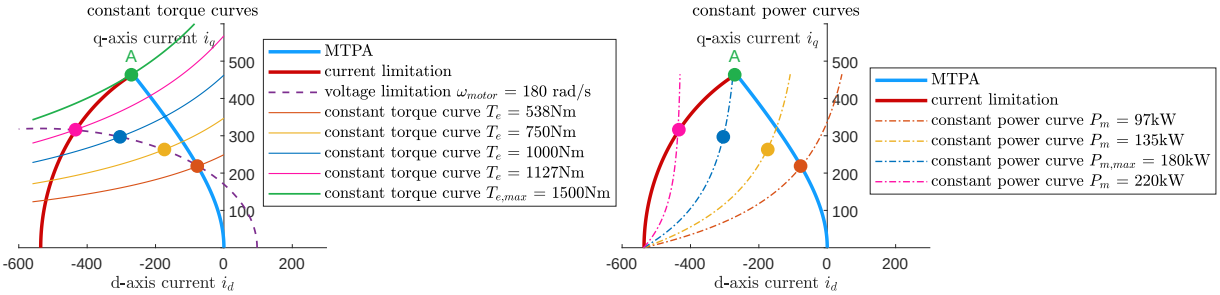

Figure 7: Comparison of four working points with the constant torque and constant power curves

3 Powertrain Structure and System Control

The motor torque and the fuel cell working point are controlled with the DC/AC gates and the DC/DC switch. Three control parts are described : the main control loop resulting into the torques commands, the drive motor control computing the DC/AC gates states (Fig.8) and the power demand apportionment managing the DC/DC switch and the transition with the load-following mode (Fig.9).

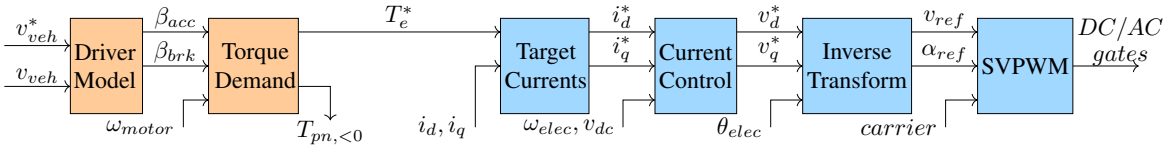

Figure 8: System control blocks : Main Control Loop and Drive Motor Control

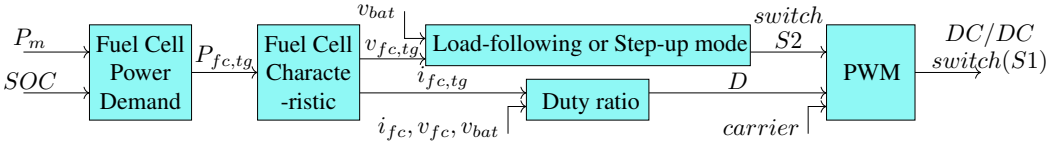

Figure 9: System control blocks : Control of the Power Demand Apportionment

3.1 Main Control Loop

3.1.1 Driver Model

The driver model is a simple closed control loop : a PI applied to the difference between the desired vehicle speed and the current vehicle speed and two saturation blocks. The acceleration pedal travel β_{acc} and the deceleration pedal travel β_{brk} are both expressed between 0 and 1.

3.1.2 Torque Demand

The bus combines a conventional pneumatic brake and a braking recovery system. The pneumatic brake torque $T_{pn,<0}$ is directly applied at the wheel when the motor torque T_e is increased with the gearbox. A function g of the rotor speed ω_{motor} is defined such that :

for $\omega_{motor} < 10$rad/s, $g(\omega_{motor}) = 0$; for $\omega_{motor} > 50$rad/s, $g(\omega_{motor}) = 1$ and g linear in between. The demand motor torque and the pneumatic braking torque are computed from the driver's pedals β_{acc} and β_{brk}. The maximum pneumatic brake is 16000Nm.

$$T^*_{e,>0} = \beta_{acc} min(\frac{P_{m,max}}{\omega_{motor}}, T_{e,max}) \quad (18)$$

$$T^*_{e,<0} = (-1)\beta_{brk} g(\omega_{motor}) min(\frac{P_{m,max}}{\omega_{motor}}, T_{e,max}) \quad (19)$$

$$T_{pn,<0} = (-1)\beta_{brk} |T_{pn,max}| \quad (20)$$

Rate limiters are applied on the torque demand to prevent current peaks. For $T_{e,>0}$, the rate is 4500Nm/s for acceleration and 6000Nm/s for deceleration. For regenerative braking the rate is 6000Nm/s and 10000Nm/s to stop. Without the function g, constrained by the rate limiter, some unwanted braking torque may cause speed error and fast changeovers between accelerations and decelerations. Fig.10 shows the small acceleration and motor regenerative braking with and without a rate limiter.

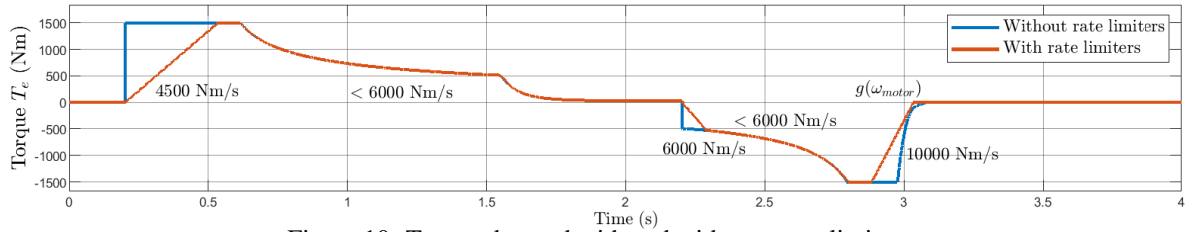

Figure 10: Torque demand with and without a rate limiter

3.2 Drive Motor Control

The motor control algorithm is a field-oriented control (FOC).

3.2.1 From the Target Torque to the Target Currents

As mentioned, the target currents are dependent of the torque demand and the motor speed. Fig.11 and Fig.12 illustrate the 2D lookup tables used to get (i^*_d, i^*_q) from (T^*_e, ω_{motor}). The motor currents evolve along the MTPA curve for low speed and in the area defined between the MTPA curve and the $P_{m,max}$ constant power curve for high speed. Some part of the matrices are empty, corresponding to excessively high powers. To place the working points inside the ellipse and not at the limit's border, some margins are taken like using the currents defined for a higher speed voltage limit. To make things easier when the voltage ellipse area becomes quite small, at very high speeds, the currents are chosen along the constant $P_{m,max}$ power curve. For regenerative braking, i_q takes the sign of T^*_e, and an another motor quadrant is in this way defined from the same look up tables.

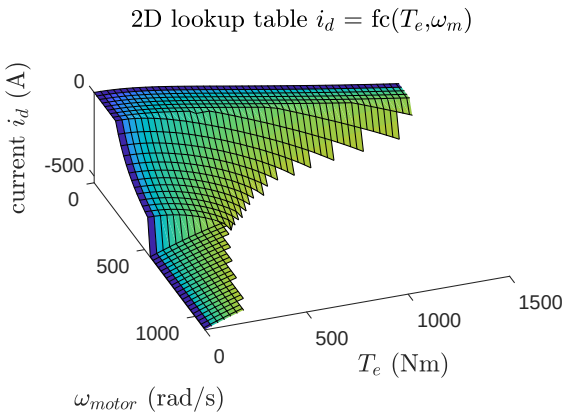

Figure 11: 2D lookuptable for the d axis current

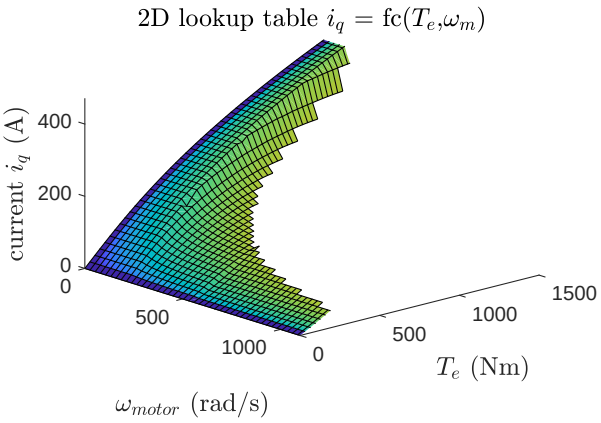

Figure 12: 2D lookuptable for the q axis current

3.2.2 Current Control

The actual motor currents i_a, i_b, i_c are transformed into d,q quantities with the DQ0 transform (4). The current control is mainly two PI regulators with the inputs $i_{d,tg} - i_d$ and $i_{q,tg} - i_q$ (the feedback control part). The cross coupling components terms $-\omega_{elec} L_q i_q$ and $\omega_{elec}(L_d i_d + \Phi_f)$ in (9) and (10) should be taken into account in the computation (the feedforward control part). Implementing the current decoupling has a very good benefit of limiting harmonic distortion. Two anti-windups are added here to deal with integrator windup risks due to the voltage limiter.

The current control computation with PIs, anti-windup and feedforward part are illustrated Fig.13.

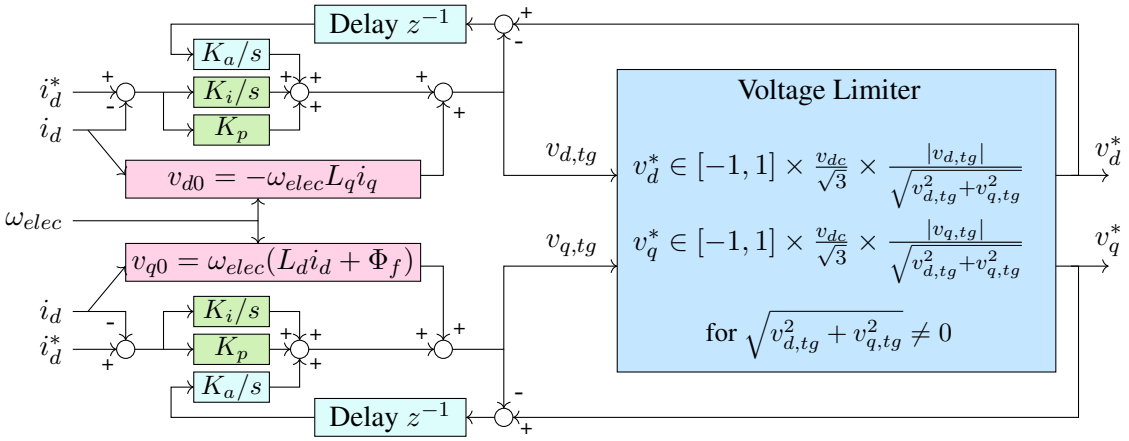

Figure 13: Chart flow to implement the current control - with current decoupling and voltage limiter [7, 6]

3.2.3 Inverse Transform

The DQ0 transform is the product of the Clarke transform and the Park transform. The inverse Park transform is applied here to get from the d,q voltages the needed quantities for the Space Vector Pulse Width Modulation.

$$\begin{bmatrix} u_\alpha \\ u_\beta \end{bmatrix} = \begin{bmatrix} \cos(\theta_{elec}) & -\sin(\theta_{elec}) \\ \sin(\theta_{elec}) & \cos(\theta_{elec}) \end{bmatrix} \quad (21) \qquad v_{ref} = \sqrt{u_\alpha^2 + u_\beta^2} \quad (22) \qquad \alpha_{ref} = atan2(u_\beta, u_\alpha) \quad (23)$$

3.2.4 Space Vector Pulse Width Modulation

A three phase inverter is composed of six switches (see Fig.14). Two switches make one leg and open and close in complementarity. Commonly, a large capacity C is placed between the real source and the three phase inverter. The load is supposed to be balanced. By switching properly the gates, an AC source could be implemented from the DC source. The voltage will have a square waveform but with a high enough switching frequency, the voltage would be a good enough approximation of a sinusoid. The eight inverter states are expressed as a binary code of the top switches (S1 S3 S5). Two space vectors are zero vectors, V_0 and V_7. Non-zero vectors form a regular hexagon in the plane (*Re*,*Im*) (see Fig.15).

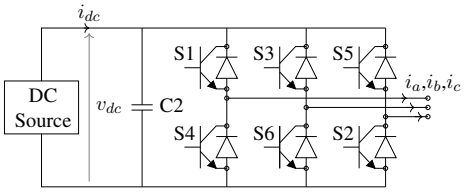

Figure 14: Three Phase Inverter with a large capacity C

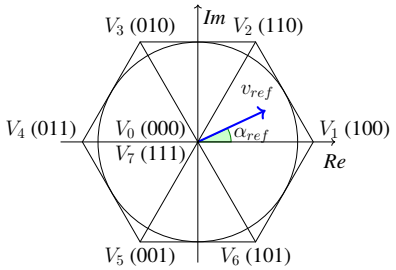

Figure 15: Spaces Vector Representation

The space vector pulse width modulation (SVPWM) consists in rotating a reference vector v_{ref} around a state diagram composed of the six non-zero vectors V_k [8]. The reference vector rotates at the frequency $f = \omega_{elec}/2\pi$ and passes through each sector. The frequency of the SVPWM (10kHz) is very large compared to the frequency f obtained in the sinusoidal approximation. Along one period of the SVPWM T_s, the reference vector v_{ref} is fixed. The angle α_{ref} determines the sector number and v_{ref} is approximated with the two state vectors of the sector. t_a and t_b are the required on-time of the active-state vectors V_k and $V_{k'}$.

$$\text{sector number } k: \quad \frac{(k-1)\pi}{3} < \alpha_{ref} < \frac{k\pi}{3} \quad (24) \qquad \overrightarrow{v_{ref}} = \frac{t_a}{T_s}\overrightarrow{V_k} + \frac{t_b}{T_s}\overrightarrow{V_{k'}} \quad (25)$$

A symmetrical pattern is chosen (the second half of the period is a reflection of the first half). The duration of the zero vectors ($t_{01} + t_{02}$) is the remaining time ($T_s - t_a - t_b$). To reduce the switching power losses, the inverter's switches are turned on and off in an optimized pattern, at each time only one bridge arm is switched. This means that somethimes $V_0V_kV_{k+1}V_7V_{k+1}V_kV_0$ is replaced by $V_0V_{k+1}V_kV_7V_kV_{k+1}V_0$.

The inverter's gates switching occurs only at a time proportional to dt, the smallest sample time of the simulation. Then $t_a/2$, $t_b/2$, $t_{01}/2$ and $t_{02}/2$ are computed proportional to dt.

Table 5:
Optimized switching patterns

Sector	Switching Pattern
1	$V_0V_1V_2V_7V_2V_1V_0$
2	$V_0V_3V_2V_7V_2V_3V_0$
3	$V_0V_3V_4V_7V_4V_3V_0$
4	$V_0V_5V_4V_7V_4V_5V_0$
5	$V_0V_5V_6V_7V_6V_5V_0$
6	$V_0V_1V_6V_7V_6V_1V_0$

$$t_a = \frac{\sqrt{3}T_s|\overrightarrow{v_{ref}}|}{v_{dc}}\cos(\alpha_{ref}+\alpha_a) \quad (26)$$

$$t_b = \frac{\sqrt{3}T_s|\overrightarrow{v_{ref}}|}{v_{dc}}\cos(\alpha_{ref}+\alpha_b) \quad (27)$$

Table 6: Angles α_a and α_b for the required times t_a, t_b calculation

Sector	α_a	α_b
1	$\pi/6$	$3\pi/2$
2	$7\pi/6$	$11\pi/6$
3	$3\pi/2$	$5\pi/6$
4	$\pi/2$	$7\pi/6$
5	$5\pi/6$	$\pi/6$
6	$11\pi/6$	$\pi/2$

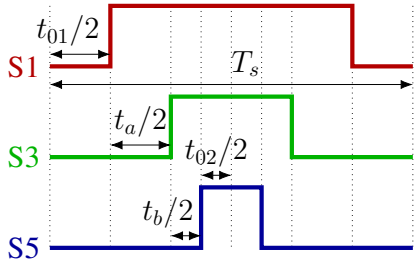

Figure 16: Example of switching sequence (sector 1)

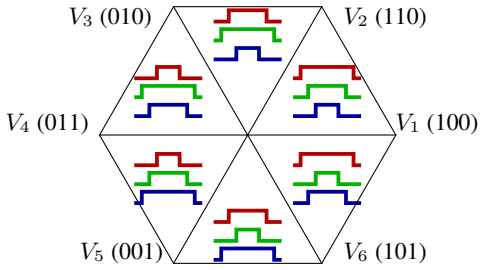

Figure 17: Switching patterns for the six sectors [8]

A carrier, a saw teeth signal of period T_s, is used to determine the step changes for the gate signals. With $V_{peak} = 2v_{dc}/\pi$ the peak value of square voltage wave, the modulation index m is $|\overrightarrow{v_{ref}}|/V_{peak}$. Three operation domains of SVPWM exist, sorted by the modulation index: the undermodulation, overmodulation mode 1 and overmodulation mode 2. The undermodulation region is the inner circle on Fig.15. The SVPWM method is often chosen in order to achieve minimum harmonic distorsion and a more efficient use of the DC supply voltage. However each modulation region has its own algorithm and only the undermodulation region algorithm is implemented in this current work.

3.3 Control of the Power Demand Apportionment

3.3.1 Fuel Cell Power Demand

The fuel cell fulfills the average power requirement of the electric motor and the compensation power for the battery charge sustaining, function of $SOC_{tg} - SOC$ [9]. A flat power demand enhances the fuel cell durability then the high frequency part of the load demands will be managed by the battery. The fuel cell power demand is bounded between 0 and 80kW and filtered with a second order low pass filter. From the power demand $P_{fc,tg}$ and the characteristic curve, if needed, the current $i_{fc,tg}$ and voltage $v_{fc,tg}$ are determined from lookup tables. Estimations of the DC/DC efficiency η_d and the inverter-and-motor efficiency η_m are used in the computation loop.

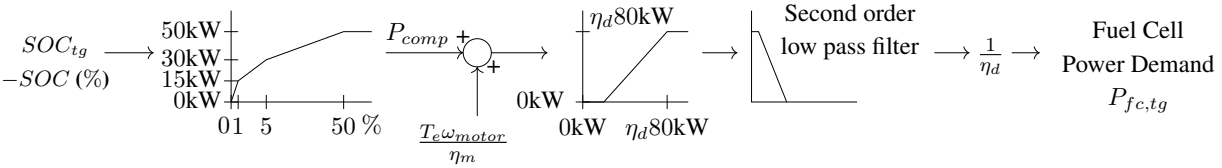

Figure 18: Steps for fuel cell power demand computation

3.3.2 DC/DC Converter

The rated voltage of the sources are close enough to only require a low voltage gain converter : the duty ratio is always below 0,3 and the gain v_{bat}/v_{fc} below 1,4. For higher voltage gain, further analysis would have been conducted to model the losses. The fuel cell is typically a low voltage high current source, the DC/DC losses can be roughly modeled by losses in a resistance, $R_{losses}i_{fc}^2$. This modeling holds the conventional step-up topology despite the retaining of large voltage stress across the switch and large blocking voltage for the output diode.

In the literature, the duty ratio of a step-up DC/DC converter is classically computed from:

$$D = 1 - \frac{v_{in}}{v_{out}} \quad (28)$$

For this specific circuit, v_{out} is the present battery voltage v_{bat} and v_{in} the target fuel cell voltage $v_{fc,tg}$.

However, an other duty ratio computation shows better simulation results [10]:

$$v_L = Dv_{in} - (1-D)(v_{out} - v_{in}) \quad (29) \qquad v_L = L\,\frac{d\,i_{in}}{dt} \quad (31)$$

$$D = 1 - \frac{v_{in} - v_{L,tg}}{v_{out}} \quad (30) \qquad V_{L,tg}(s) = (K_p + \frac{K_i}{s})[I_{in,tg}(s) - I_{in}(s)] \quad (32)$$

$v_{out} = v_{bat}$, $v_{in} = v_{fc}$, $i_{in} = i_{fc}$ and $i_{in,tg} = i_{fc,tg}$, the targeted changes are expressed through the inductance voltage $v_{L,tg}$ and the PI parameters are adjusted. With a fixed simulation sample time at 2μs and the PWM period at 100μs, the duty ratio is discretized. The computed duty ratio is round up to the nearest, more or less 0,02.
Using (30) and (32), the closed control loop costs a duty ratio signal with more oscillations but achieves a smoother fuel cell voltage. See Fig.19, the duty ratio from (28) is a really nice curve but the discretization has a bad effect on the voltage.

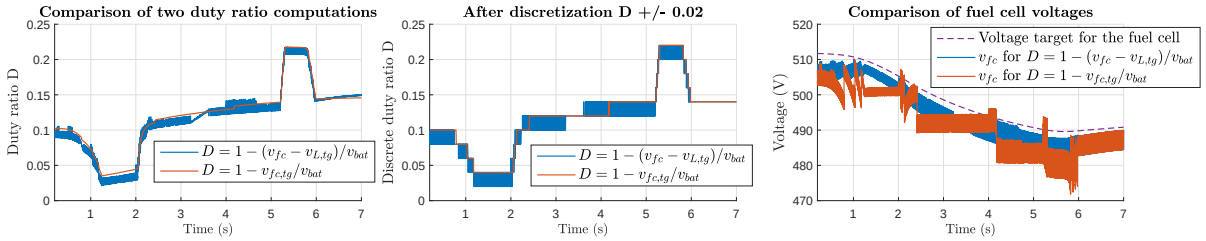

Figure 19: Comparison for two duty ratio computations

3.3.3 Load-following Mode or Step-up Mode

A controlled apportionment of the power demand between the fuel cell and the battery is only feasible through the control of the DC/DC. With the direct path, the fuel cell working point is driven by the load. With the step-up converter, the fuel cell voltage drops under the battery voltage and is controlled with the duty ratio. The transition from one to another mode (load-following or DC/DC) is based on the comparison between the target fuel cell voltage and the battery voltage. The switch S2 is flipped as follows:

$$S2 = 1 \Leftrightarrow v_{diode} + v_{bat} \leq v_{fc,tg} \quad (33)$$

The gate signal of switch S1 is built with the duty ratio, a saw teeth carrier and the complementary of S2.

3.4 Multi Scale Modeling

With the help of Matlab/Simulink zero order hold and rate transition blocks, parts in the model are operating at different rates. The sample time is 2μs for the electrical variables and converters gates, 1ms for the driver model, gearbox and vehicle dynamic, 100μs for the d,q quantities and 500μs the motor torque command. With these rates, the simulation quickly reaches a point of storage shortage. A 1800s modeling is achieved by concatenation of the desired data, in practice using 20s samples. The computation time is around four hours with an Intel i7 2.6GHz computer.

4 Simulation

With the components modeled and the control algorithm previously introduced, this work is now a tool to link powers, torques, currents and voltages on the one hand and battery and fuel cell behavior for long driving cycle on the other hand.

4.1 Example 1 : a small acceleration and braking

Fig.20 shows how the battery and the fuel cell react for a small acceleration and regenerative braking.

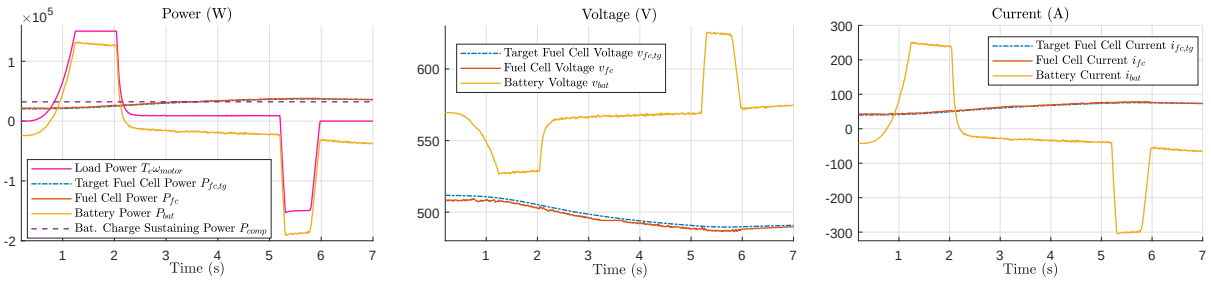

Figure 20: Powers, voltages and currents for a small acceleration and braking ($P_{fc,init}$ = 20kW)

The target fuel cell power increases slowly (low pass filter at 0.05Hz). The load power is initially null and the fuel cell delivers power to charge the battery. During the acceleration process, the load power reaches 150kW. The battery fulfills this power demand minus the present fuel cell power. The battery current increases and the battery voltage drops. The fuel cell current and power carefully follow the targets, while the fuel cell voltage has a small gap of 2 or 3V with the voltage computed from the fuel cell characteristic curve. The battery charges again thanks to the fuel cell and the regenerative braking power, increasing the voltage and decreasing the current.

4.2 Example 2 : CWTVC driving cycle

The CWTVC driving cycle is an example for heavy duty vehicles. First the vehicle speed matches very well the target (Fig.22) at the cost of an uneven motor torque demand (Fig.23). When the vehicle speed reaches 52km/h, the gearbox switches the ratio and the rotor speed has step changes (see Fig.24 at 105s, 675s, 709s, etc.). For this example the initial battery SOC is 45%, below the target SOC_{tg}. The fuel cell gives more energy to recharge the battery but starting from 1200s, more torque is requested and the battery is depleted (Fig.25).
Due to cross coupling components, the q-axis voltage v_q is sensible to the large changes of i_q and the gearbox shifting disturbs the d,q axis voltages (Fig.26 and Fig.27). i_q is here always below 120A, that means the area close to point A is not used in this example, the torques are quite low due to the rotor speed range. v_d and v_q reach both positive and negative values : v_d lies between -220V and 61V and v_q between -14V and 254V.

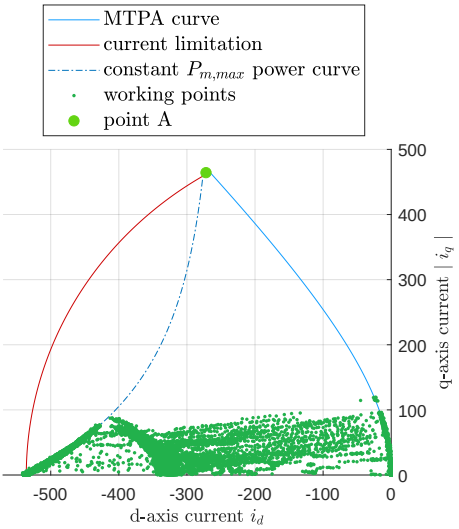

Figure 21: d,q motor currents working points in the plane (i_d,i_q)

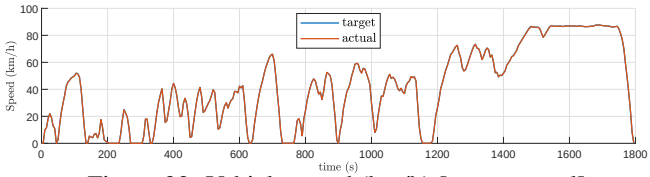

Figure 22: Vehicle speed (km/h) [target,actual]

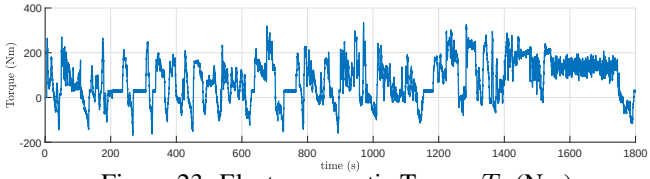

Figure 23: Electromagnetic Torque T_e (Nm)

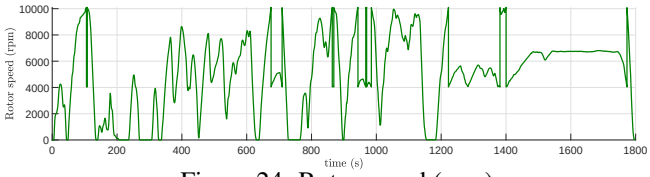

Figure 24: Rotor speed (rpm)

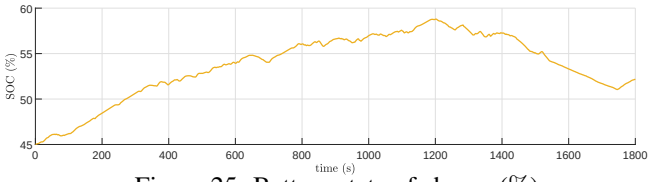

Figure 25: Battery state of charge (%)

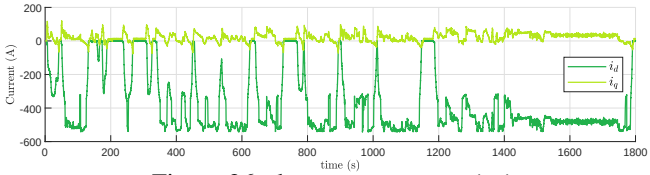

Figure 26: d,q motor currents i_d,i_q

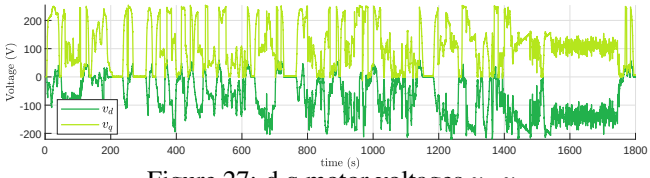

Figure 27: d,q motor voltages v_d,v_q

The voltage battery v_{bat} is equal to the DC source voltage v_{dc}. This modeling gives a tool to examine the DC/AC inverter and motor drive quantities without having the simplifying assumption of a steady DC voltage source (Fig.28). For this example, the fuel cell is used to charge the battery. This makes the fuel cell voltage lower than the battery voltage and the direct path is almost not used. With v_{bat} and v_{fc} close enough, the voltage gain is below 1,25 and the duty cycle below 0,2 (Fig.29).
High frequencies load are deemed less harmful for the battery than for the fuel cell stack. Still the obtained changeovers are very demanding for the battery (Fig.30). The fuel cell power has effectively a low frequency behavior (Fig.31). However a steadier power command could be well received, further adjustments could be wished in the modeling control part.
The energy from/to each components in the modeled powertrain is shown Fig.32. First, the braking recovery is a little less than expected. Second, the estimated losses for the DC/DC, battery, inverter and electric motor are reasonably low. Thereafter, regarding the battery, more energy is given to than taken from the battery (12,3MJ for 1800s), which corresponds to a rise of 7.2% for the SOC. This modeling as of now only takes into account the fuel cell current and voltage at the left side of the electrical circuit given Fig.3. Achieving an efficiency superior to 55% (including the DC/DC) imposes having the fuel cell engine efficiency superior to 0,56. The fuel cell engine delivers at the electrical circuit input a maximum power of 80kW. This means the fuel cell stack gives before a higher power to deal with the accessorial stack components like the cooling fans and water pumps.

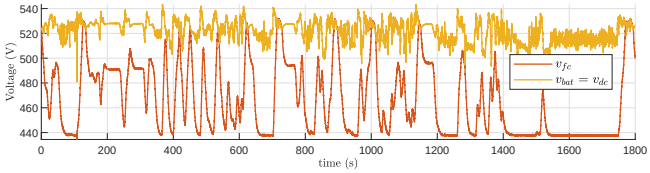

Figure 28: Fuel cell and battery voltages

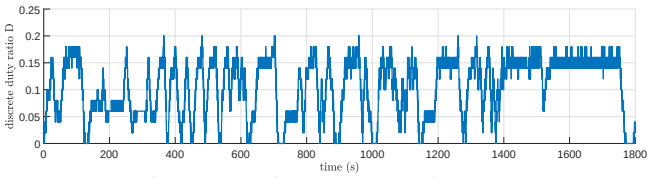

Figure 29: Discrete duty ratio D

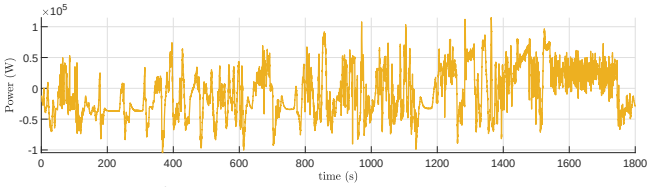

Figure 30: Battery power (W)

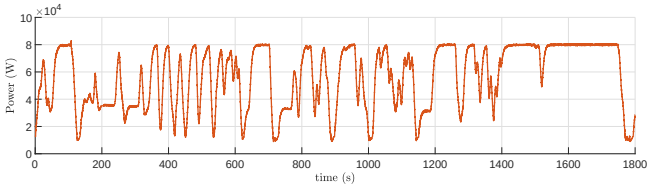

Figure 31: Fuel cell power (W)

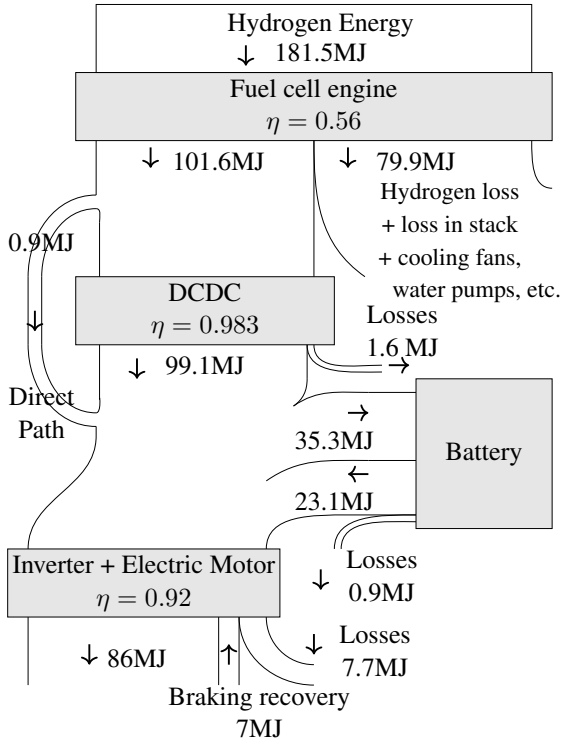

Figure 32: Energy flow diagram

Conclusion

This work presents a multi-scale modeling for a fuel cell highway bus prototype. It is mainly expected as a relevant simulation tool to access the powertrain currents, voltages, powers, torques, speeds, switches states, etc. This article reports the main methods and control parts usable to redo such a modeling. From vehicle's wheel to converters switches, this modeling work includes several sizes and frequencies. The components models work at different rates to deal with this modeling inherent problematic. The motor is powered by two different sources, therefore a power split strategy algorithm is defined, respecting as much as possible some safeguard principles for the preservation of the fuel cell system lifespan. Further measurements and tests would be used to improve this simulation tool, by comparing modeling results and experimental data. A more sophisticated model would also be implemented for the fuel cell stack and the battery.

References

[1] Fuel cell system degradation analysis of a Chinese plug-in hybrid fuel cell city bus. *International Journal of Hydrogen Energy*, 2016.

[2] Jiuyu Du, Minggao Ouyang, and Jingfu Chen. Prospects for Chinese electric vehicle technologies in 2016 - 2020: Ambition and rationality. *Energy*, 2017.
[3] Liangfei Xu, Fuyuan Yang, Jianqiu Li, Minggao Ouyang, and Jianfeng Hua. Real time optimal energy management strategy targeting at minimizing daily operation cost for a plug-in fuel cell city bus. *International Journal of Hydrogen Energy*, 2012.
[4] Hu Zunyan, Li Jianqiu, Xu Liangfei, Song Ziyou, Fang Chuan, Ouyang Minggao, Dou Guowei, and Kou Gaihong. Multi-objective energy management optimization and parameter sizing for proton exchange membrane hybrid fuel cell vehicles. *Energy Conversion and Management*, 2016.
[5] MATLAB. *version 9.5 (R2018b)*. The MathWorks Inc., Natick, Massachusetts, 2018.
[6] Sang-Hoon Kim. *Electric Motor Control : DC, AC, and BLDC Motors*. 2017.
[7] MATLAB Examples : IPMSM Torque Control. MATLAB Command : pe_ipmsm_torque_control (2017).
[8] Phuong Hue Tran. Master thesis, MATLAB/Simulink implementation and analysis of three pulse-width-modulation (PWM) techniques, 2012. unpublished thesis.
[9] Liangfei Xu, Minggao Ouyang, Jianqiu Li, and Jianfeng Hua. Hierarchical control of vehicular fuel cell / battery hybrid powertrain. *EVS25 Shenzhen, China*, 2010.
[10] Mamadou Baïlo Camara, Hamid Gualous, Frederic Gustin, and Alain Berthon. Design and new control of DC/DC converters to share energy between supercapacitors and batteries in hybrid vehicles. *IEEE Transactions on Vehicular Technology*, 2008.

Authors

Marion Georges, student from CentraleSuplec Engineering School (France), is currently in a double degree for a 2-year Master Degree at the Department of Automotive Engineering, Tsinghua University (China).

Liangfei Xu received the PhD degree in power engineering and engineering thermos physics at Tsinghua University in 2009. Since 2017, he is an Associate Professor with the Department of Automotive Engineering. His research interests cover the arears of dynamics and control of polymer electrolyte membrane (PEM) fuel cells and fuel cell electric vehicles. He won the 5th ProSPER.NET-Scopus Young Scientist Award (2013), the China Industry-University-Research Institute Collaboration Innovation Award (2018), and is an Alexander von Humboldt Fellow (since 2015).

Bingkun Cai received the B.E. degree in automotive engineering from Tsinghua University, Beijing, China, in 2017, where he is currently working toward the master's degree with the State Key Laboratory of Automotive Safety and Energy, Department of Automotive Engineering. His research interests include parameter estimation and control of motor and sensor signal processing.

Jiayi Hu received the B.E. degree in automotive engineering from Tsinghua University, Beijing, China, in 2017, where he is currently working toward the Ph.D. degree with the State Key Laboratory of Automotive Safety and Energy, Department of Automotive Engineering. His research interests include electric and hybrid electric vehicle systems, in-wheel motors, and vehicle dynamics and control.

Jianqiu Li received the PhD degree in power engineering and engineering thermos physics at Tsinghua University in 2000. Since 2010, he is a full Professor with the Department of Automotive Engineering. His research interests cover the areas of PEM fuel cells and powertrains, hybrid and electric vehicles, in-wheel electric motors and distributed drivelines. He is supported by the National high level talents special program (Ten thousand plan) since 2017, the vice director of the State Key Lab of Automotive Safety and Energy, and the leader of the hydrogen fuel cell research group at Tsinghua.

Minggao Ouyang received the PhD degree in energy and power engineering at the Technical University of Denmark in 1993. Since 1998, he is a full Professor with the Department of Automotive Engineering at Tsinghua University in Beijing, China. He established the scientific research group of new energy powertrains at Tsinghua, and his research interests cover the arears of advanced internal combustion engines and hybrid systems, power batteries, PEM fuel cells and electric vehicles. He founded the international journal *eTransportation* in 2018. He is the Yangtze river scholars Distinguished Professor (since 2004), the vice director of Tsinghua Academic Committee (since 2008), and the China Scientific Academician (since 2018).